Geometry-dependent modal field properties of metal-rod-array-based terahertz waveguides

doi: 10.1364/OSAC.2.000655

Research Article Vol. 2, No. 3 / 15 March 2019 / OSA Continuum 655
OSA CONTINUUM

Geometry-dependent modal field properties of metal-rod-array-based terahertz waveguides

DEJUN LIU,[1] JA-YU LU,[2] BORWEN YOU,[1,3] AND TOSHIAKI HATTORI[1,4]

[1]Department of Applied Physics, University of Tsukuba, Tennodai 1-1-1, Tsukuba, Ibaraki 305-8573, Japan
[2]Department of Photonics, National Cheng Kung University, No. 1 University Road, Tainan 70101, Taiwan
[3]you.borwen.gt@u.tsukuba.ac.jp
[4]hattori@bk.tsukuba.ac.jp

Abstract: One terahertz (THz) waveguide based on the metal rod array (MRA) structure is numerically demonstrated in 0.1–1 THz, including the fundamental and high-order transverse magnetic (TM) modes. The high-order TM-mode THz waves are strictly confined inside the MRA structure and are thus sensitive to the metal rod interspace for their spectral positions, bandwidths, transmittances, and attenuation coefficients. Arranging metal rods with fine-tuning the interspaces across the optic axis is presented as the critical stratagem to optimize the transportation efficiency of THz waves through an MRA structure. The maximum propagation length of MRA-confined THz waves is over 30 mm with the lowest attenuation coefficients of approximately 0.05–0.1 cm^{-1}. The MRA is, therefore, applicable as one deformable artificial structure in THz frequency region because simply one-axial adjustment of the metal-rod interspace enables the modulation purpose without uniform adjustment on the two-dimensional metal rod interspace.

1. Introduction

Periodic metal structures are adopted to manipulate electromagnetic (EM) waves at different frequency regions on chips [1]. For the waves at ultraviolet, visible and infrared (IR) spectra, the metal structures with approximate interspace sizes enhance the coupling efficiency from the EM wave into surface plasmon polaritons (SPPs) or plasmonic surface waves (PSWs) [2,3]. The PSWs are specified as the propagation waves on the metal surfaces, consisting of SPPs and the waveguide modes bound in the periodic structures [4]. For PSWs on metal surface structures with extremely low frequencies at far IR, terahertz (THz), and microwave spectra, their waveguide dispersion features approximate those of pure metal SPPs, which are called spoof SPPs [5]. The periodic metal structures used for the optical chip system can thus confine EM waves and transport certain photons as waveguide channels [6–9].

EM waves in 0.1–1 THz frequency can be easily obtained with high signal-to-noise power ratios ($>10^5$) based on the mature technology of high-peak power lasers and time-domain spectroscopic systems. Given that subwavelength-scale metal structures of 0.1–1 THz waves are easily fabricated by laser scribing or photolithography, diverse metal patterns are developed as THz metasurfaces due to the abnormal optical properties in THz frequency spectrum [10]. Schemes of multi-stacked metasurfaces have also been presented, although their waveguide capabilities are hindered from dielectric substrates and inappropriate metal patterns without waveguide modes for long-distance propagation [11]. Transverse magnetic (TM) waveguide modes exist at periodic metal slits (or slots) when the input THz wave polarization is perpendicular to the long axis of slit [12]. Such TM waveguide modes of slits transport the input THz waves without being limited by the subwavelength-scaled slit widths [13]. Conversely, THz waves are strongly reflected from the subwavelength-scaled metal slits for input THz waves with polarization parallel to the long axes of slits, which corresponds to the transverse electric (TE) polarization [14]. To apply the TM waveguide modes of metal slit array for long-distance propagation, the

#352109 https://doi.org/10.1364/OSAC.2.000655
Journal © 2019 Received 16 Nov 2018; revised 26 Jan 2019; accepted 27 Jan 2019; published 1 Mar 2019

OSA CONTINUUM

free-standing metal rod array (MRA) structure has been experimentally demonstrated in 0.1–1 THz for a photonic crystal (PC) waveguide [15,16]. Experimental investigation has indicated that 0.1–1 THz waves that input an MRA can be divided as the fundamental and high-order waveguide modes by one apparent rejection band [16]. Such an MRA-rejected spectrum is resulted from the Bragg reflection and consistent to the equation of the 1st-order Bragg law. This is the proof to reveal that an MRA has a PC bandgap, resembling one kind of PC in THz frequency region.

Using one MRA structure to guide THz waves should work via the edge coupling configurations as dielectric slab waveguides, which is different from those corrugated metal waveguides with normal coupling configuration [17,18]. The excited transverse fields on the corrugated metal waveguides, i.e., spoof SPPs, cannot propagate long distances due to their strong confinement with high loss. The MRA-guided waves with THz frequency above the 1st-order Bragg band are approved in experiments with high lateral confinement at the metal-rod tips and the long distances over 12 mm [16]. The MRA slab waveguide is thus better than those corrugated metal waveguides to guide surface-confined THz waves. However, for the concept of waveguide subwavelength structures [19], the high-frequency transmission bands of PC are the radiation modes without significant modal fields to guide for a long distance. Therefore, the theoretical waveguide properties of MRA-PC dependent on the geometry and THz frequency should be further figured out when the MRA structures would be applied for waveguides. The interspace sizes of MRAs have been uniformly adjusted, e.g., G_x=G_y, in the experiments to observe various photonic bandgaps within 0.6 THz [15,16], but the adaptability of asymmetric interspaces, e.g., $G_x \neq G_y$, for waveguide modes is not revealed.

In this study, the spectral properties of waveguide entrance and rejected band are first calculated by the finite-difference time-domain (FDTD) method to, respectively, determine the wave polarization and metal-rod length for the MRA waveguide modes. Based on the TM modes of the parallel metal plate waveguides (PPWGs) and the effective medium concept, the FDTD simulation illustrates that the metal rod interspace across the optic axis enables one modulation method for 0.40–0.70 THz wave transmission through an MRA, including the bandwidth, lateral confinement, and attenuation. The simulation results finally indicate that MRA-based THz artificial medium is deformable simply via one axial control and can be realized as one optomechanical modulators for modal-field confinement or spectral filters. Such one axial control of MRA structure is robust and precise on a microelectromechanical system because two-axial adjustment on the MRA-interspace is very difficult to achieve the engineering requests of high-uniformity and high-speed.

2. Deformable scheme of MRA waveguide

The MRA configuration is schematically depicted in Fig. 1 (a) and consists of uniform metal rods to form 13 lines and 30 layers of rod array along the X- and Y-axes, respectively. The 13-line width makes the MRA structure resemble one slab waveguide to receive one THz beam size with a diffraction limit in 0.1–1 THz. The 30-layer length is specially considered as a workable propagation length to perform the PC waveguide properties [16]. The metal rod has a distinct aspect ratio with 1 mm length and 0.16 mm diameter (D), which are obtained from the mature fabrication parameters in the micro-stereolithography and sputter coating methods [15,16]. It represents that the uniformity of a 0.16 mm diameter can be sustained along one 1 mm-rod length during the micro-stereolithography construction. Based on a 0.16 mm-rod diameter and a 13×30 array dimension, this simulation work presents one stratagem to adjust the X-axial interspace (G_x) but maintains the Y-axial interspace (G_y) to modify the waveguide capability along an MRA structure. G_y is fixed at 0.26 mm, whereas G_x is adjusted in the range of 0.08–0.50 mm. Figure 1(b) illustrates that the fine-tuning stratagem of G_x can be considered as the deformable property of MRA. Each MRA line structure along Y axis can be fabricated as one module and periodically assembled along X-axis with piezo actuators on the substrate. The G_x value thus can

OSA CONTINUUM

be adjusted by various driving voltages, which is denoted as G_x(V) in Fig. 1(b). The interacted layer number and the G_y value are the constants based on the scheme of MRA-line structural module.

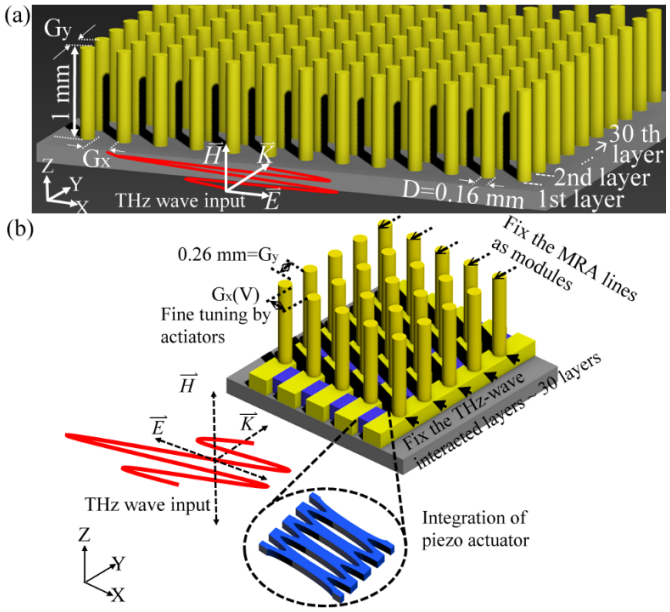

Fig. 1. (a) Waveguide configuration based on an MRA structure. (b) The deformable concept of an MRA.

3. Numerical results

In the FDTD simulation of MRA waveguides, the material of the rod is considered a perfect electronic conductor (PEC) and the input wavefronts belong to the Gaussian beams. The theoretical transmission spectra and field distributions are presented in the numerical results to observe the MRA-geometry-dependent waveguide properties. The waveguide modes of one-layer MRA is initially discussed to reveal the existence of TM waveguide modes at the array entrance layer [i.e., the 1st MRA layer in Fig. 1(a)]. The waveguide spectrum and confinement of MRA are then discussed.

3.1. Waveguide modes of one-layer MRA

For the PEC material of the metal rod, THz waves cannot penetrate the rods and only distribute outside the rods. Thus, the MRA-guided THz field is simply distributed in the rod interspace or on the metal rod surface but not inside the metal rod. When TE- and TM-polarized THz waves irradiate the interspace among the metal rods in the X–Z plane (i.e., the G_x interspace in one-layer MRA; Fig. 1(a)), their transmittance spectra are different. One interspace of G_x in one-layer MRA is thus the structural unit to determine the MRA transmission spectrum.

The 0.26 mm G_x is taken as an example to express the characteristics of TE- and TM-polarized waves through the interspace of one-layer MRA. The electric/magnetic field directions of TE, TM waves, and the corresponding transmittance spectra are presented in Fig. 2(a). The calculated transmittance involves the coupling loss of a Gaussian beam spot with a 1 mm diameter and the propagation loss along one layer of MRA. The transmittance spectra of one-layer MRA have the same features with those of a metal slit [14]. The common features of TE wave transmission for

OSA CONTINUUM

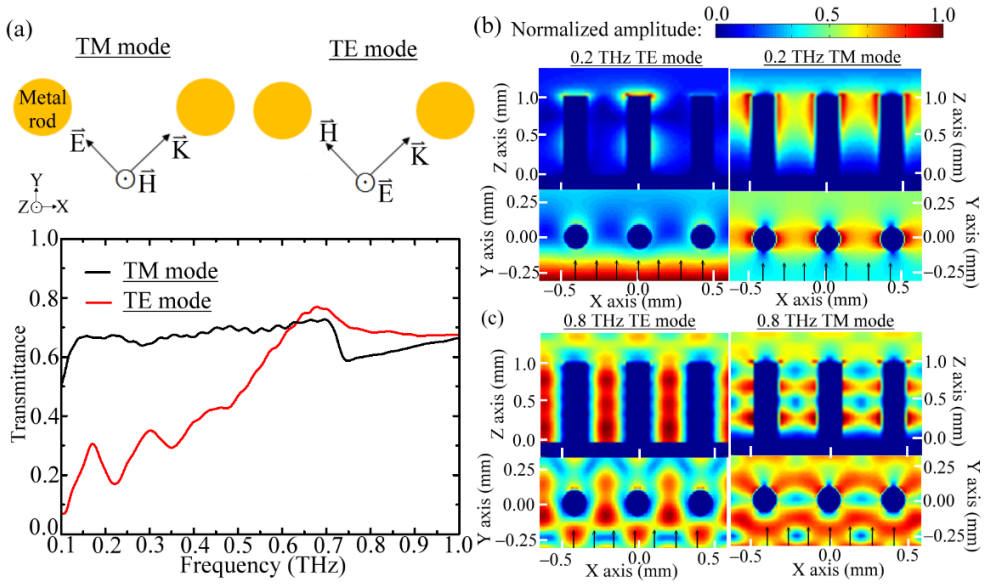

Fig. 2. (a) Transmittance spectra of TE and TM modes through one-layer MRA. Electric field distribution of TE and TM modes outputted from one-layer MRA for (b) 0.2 and (c) 0.8 THz waves.

the metal slit and metal rod interspace are the high-frequency pass spectrum and one apparent spectral peak due to across-resonance effect. The spectral peak of MRA with 0.26 mm G_x is at 0.7 THz, and G_x is approximately one-half wavelength of the 0.7 THz wave [14].

The TM-mode transmission of MRA with 0.26 mm G_x performs a wide bandwidth. As shown in Fig. 2(a), such a wide bandwidth certainly covers the range of at least 0.1–1 THz; however, one discontinuous transmittance at 0.7 THz exists, which is also resulted from the across-resonance effect of the X-axis for the TM wave transmission. The transmittance difference between the TE and TM modes in 0.1–0.7 THz originates from the existence of the waveguide mode. For example, the electric field of the TM wave can be accumulated on the metal rod surface and observed in the X–Y plane of the rod tip, as shown in the 0.2 THz wave in Fig. 2(b). However, the electric field of 0.2 THz TE wave is stopped by the MRA layer without apparent field observed at the output X–Z plane. [Figure 2(b)].

For THz frequencies above 0.7 THz, TE wave can pass through the MRA layer and perform the approximate transmittance with that of the TM waves [Fig. 2(a)]. The electric field distribution of TE waves above the 0.7 THz frequency is different from that of TM waves. For example, the 0.8 THz TE wave performs the high field density at the rod interspace, as shown in the X–Y plane in Fig. 2(c); however, the field of TM wave accumulates on the metal surface. Along the rod or the Z-axis, a 0.8 THz TM field accumulation is separated as three spots, in contrast to the uniform distribution of the TE wave shown in the X–Z plane of Fig. 2(c). The TM field accumulation along the rod and in the X–Z plane represents the waveguide modal pattern of the across interspace. The TM field at 0.8 THz thus has the high-order waveguide mode [Fig. 2(c)]. By contrast, the 0.2 THz TM wave in Fig. 2(b) has a single field spot in the Z-axis and is indicated as one fundamental waveguide mode. The experiments also show the TE wave propagation length of MRA is only three layers, much shorter than that of the TM wave [15,16].

3.2. *Waveguide spectrum of MRA*

The output TM waves from one-layer MRA with 0.26 mm G_x is further investigated to interact with the other multiple layers. In this case, additional 29 MRA layers with 0.26 mm G_x are

OSA CONTINUUM

periodically integrated with the Y-axial interspace (G_y) of 0.26 mm [i.e., G_x=G_y=0.26 mm, Fig. 1(a)]. Figure 3(a) shows the transmission spectra for the 30 MRA layers using 2D and 3D frameworks of FDTD calculation, denoted as red and blue curves, respectively. All the structural dimensions of the MRA are consistent between the conditions of 2D- and 3D-FDTD calculations; however, the Z-axial rod lengths are different, which are infinite and 1 mm, respectively.

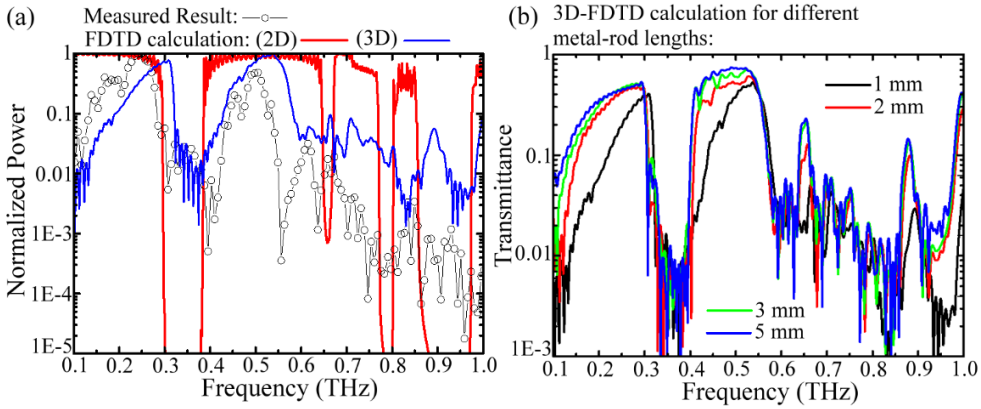

Fig. 3. (a) Transmission spectra for a measured result [16], 2D- and 3D-FDTD calculations. (b) Calculated transmittance spectra based on 3D-FDTD for different metal rod lengths of MRAs

The 3D-FDTD spectrum is approximate to the measured one in the literature [16] [Fig. 3(a)]. Thus, one rejection band is contributed by the added 29 MRA layers to divide the wide bandwidth of the 1st MRA layer [Fig. 2(a)]. The rejection band in the 3D-FDTD calculation is at 0.32–0.42 THz, which is close to that obtained in the 2D-FDTD calculation. The 2D- and 3D-FDTD results follow the Bragg law when various equidistant interspaces integrating the 0.16 mm D rod (i.e., various structural periods and G_x=G_y) are considered in the FDTD calculation. However, only the 1st Bragg order occurs for 3D-FDTD calculation result on the basis of the 1-mm-long metal rods [16]. The high-order reflection of the Bragg-like waves is performed at 0.65, 0.80, and 0.9 THz by the infinite metal rod length, as presented in the result of the 2D-FDTD calculation [Fig. 3(a)]. The 3D-FDTD results indicate that the waves higher than 0.58 THz and without Bragg-like reflection strongly radiate away from the 1-mm-long metal rods. In other words, TM waves above 0.58 THz are not guided through the 30 MRA layers with 1-mm-long metal rods. The 3D-FDTD simulation of Fig. 3(b) reveals that the high-order reflection of Bragg-like waves, >0.58 THz, only occurs for the metal rod length longer than 2 mm, but their transmittance is considerably low with narrow bandwidths. For the waveguide modes with frequency less than 0.58 THz [Fig. 3(b)], the corresponding waveguide transmittance obviously increases with metal rod length.

3.3. Modal field confinement of MRA-based waveguide

In this section, the electric field distributions of TM waves in the X–Z plane behind the 30th MRA layer are calculated by 3D-FDTD to characterize the frequency-dependent modal fields, where the MRA interspaces are equidistant at 0.26 mm. As shown in Fig. 4(a), the detected THz wave power at the cross section of the MRA output end is integrated from the X-Y plane and presented as a function of Z factor in the range of 0.85–1.15 mm. Given that the bottom and tip of the rod are 0 mm and 1.0 mm at the Z-axis, respectively [Fig. 1(a)], the Z-axial power observation at 0.85–1.15 mm can confirm the lateral-field confinement of waveguide surrounding the metal-rod tips.

OSA CONTINUUM

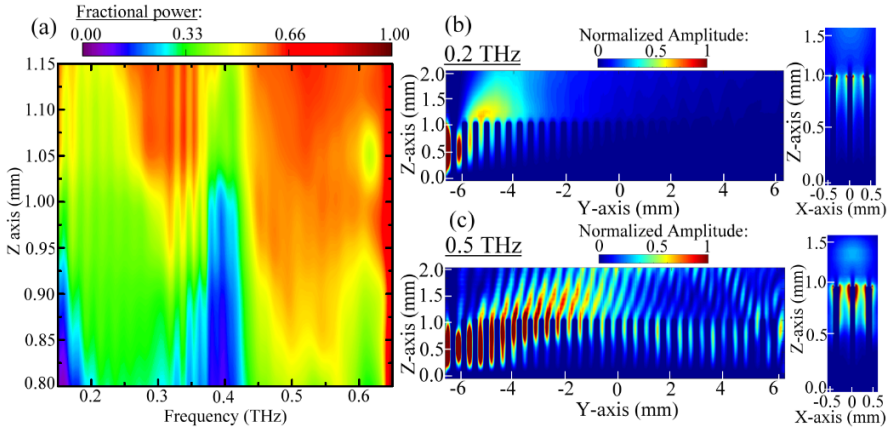

Fig. 4. (a) Frequency-dependent modal power fraction of the 30-layer MRA waveguide (G_x=G_y=0.26 mm). Electric field distributions of (b) 0.2 and (c) 0.5 THz waves in the Y–Z and X–Z planes.

The waves in 0.15–0.25 THz are deliverable through the 30 MRA layers [Fig. 3(a)]; however, the fractional power inside the MRA is only 0.33, which is considerably lower than that of the waves in 0.45–0.58 THz. For the waves in 0.25–0.32 THz, the waveguide power fraction higher than 0.6 is guided near the rod tips but still outside the MRA structure, that is, in the air cladding for Z > 1.0 mm. The calculation result of the power fraction shows that the TM waves lower than the Bragg rejection band in 0.15–0.32 THz cannot be confined inside the MRA structure; these waves are called the leaky waveguide modes via TM wave irradiation on the entrance layer of the MRA. Figure 4(b) shows a 0.2 THz wave for its electric field distribution in the Y–Z planes at the center of the X-axial MRA and the waveguide output modal pattern in the X–Z plane. Most of 0.20 THz field radiates out of the MRA between the 1st and 4th MRA layers. Consequently, the transmission power fraction inside the MRA is lower than 0.33 [Fig. 4(a)]. In comparison with the waveguide modal pattern through the entrance layer [Fig. 2(b)], the waveguide modal pattern through the 30-layer MRA propagation can be preserved, as shown in the X–Z plane in Fig. 4(b).

For 0.45–0.58 THz waves, the power fraction over 0.6 is confined inside the MRA, as shown in Fig. 4(a). We take 0.5 THz wave as an example in Fig. 4(c) to observe the electric field distributions in the Y–Z plane at the MRA X-axial center and the waveguide output modal pattern in the X–Z plane. The MRA-confined field is found in the G_y interspaces along the 30-layer MRA propagation and performs a larger area on the waveguide modal pattern than that of the 0.2 THz wave in the X–Z plane [Fig. 4(b)]. The calculation result of the power fraction reveals that the TM waves with EM frequencies higher than the Bragg rejection band in 0.45–0.58 THz are exactly confined inside the MRA structure; these TM waves are called the confined waveguide modes. The spectral peak with the highest transmittance at 0.50–0.58 THz [Fig. 3(a)] has the largest power fraction, >0.6, around Z-axis position of 0.85 mm; thus, the high-order TM waveguide modes of MRA are not only confined but also have very high transmittance, obviously distinct from the waveguide properties of spoof SPPs on the corrugated metal waveguides [17,18].

3.4. *Modal field properties dependent on the asymmetrical interspaces*

The MRA waveguide irradiated by TM waves through 30 MRA layers with equidistant interspace of 0.26 mm are theoretically characterized in the transmission spectrum [the blue curve in Fig. 3(a)] and the Z-axial power confinement [Fig. 4(a)]. The 12 channels constructed by the 13 lines of MRA [Fig. 1(a)] with a uniform interspace width G_x resemble 12 channels of PPWGs.

OSA CONTINUUM

Although the periodic G_y interspaces exist to make the metal reflection surface discontinuous, they mainly modulate the Y-axial propagation constants of the TM waveguide modes to generate the Bragg rejection band. G_x is one of the geometric parameters that controls the TM mode spectrum, bandwidth, and transmittance to manipulate the TM waveguide modes of each G_x interspace channel.

On the basis of the effective medium concept, the cutoff frequency of the TM waveguide mode along one G_x interspace channel is assumed as follows:

$$\nu_c = mC/2n_{eff}G_x, \tag{1}$$

where ν_c, m, C, and n_{eff} are the cutoff frequency, number of TM waveguide mode, light speed in vacuum, and effective waveguide refractive index, respectively. For the case of 0.26-mm-G_x MRA in Fig. 3(a), the fundamental mode (m = 1) is in the range of 0.15–0.32 THz, and the one high-order mode (m = 2) occurs in 0.42–0.58 THz.

On the basis of the fixed G_y value at 0.26 mm, various G_x interspaces are calculated by the 3D-FDTD method for the transmission spectra of 30-layer MRA (Fig. 5(a)–(d)). Fundamental waveguide modes constantly exist for 0.08–0.50 mm G_x. The fundamental waveguide mode is also called the 1st TM waveguide mode. However, the high-order modes within 1 THz are critical to the G_x values for their spectral formation and positions. For a small G_x (0.08–0.14 mm) [Fig. 5(a)], two high-order modes, which are the 2nd and 3rd TM waveguide modes, i.e., m = 2 and 3, respectively, are performed around 0.6 THz and 0.8 THz. When G_x increases to 0.16–0.22 mm, the 2nd and 3rd TM waveguide modes approximately combine around 0.6 THz because of the strong redshift of the 3rd mode [Fig. 5(b)]. The 3rd TM waveguide mode finally disappears when G_x increases to 0.26–0.36 mm [Fig. 5(c)]. For the G_x in 0.38–0.50 mm [Fig. 5(d)], several waveguide modes randomly occur above the frequency of the 2nd mode without correlating to the G_x interspaces. Additionally, the transmittance spectra between the two cases of G_x=G_y and G_x≠G_y are compared in Fig. 5(e). The fundamental mode spectra are approximate when the symmetric interspace becomes the asymmetric one; contrarily, the spectra of the 2nd TM (high-order) modes can be modified by the asymmetric interspaces. Therefore, only modifying G_x interspaces on MRAs can realize THz wave modulation at the 2nd TM mode, thereby replacing the uniform adjustment of MRA interspace [16].

The cutoff frequencies of the 1st and 2nd TM waveguide modes in Fig. 5(a)–(d) are further observed in their low frequency ranges, whose transmittances are 10% of the peak values and presented in Fig. 6(a). The cutoff frequencies of the TM waveguide modes are inversely proportional to G_x. That is, the cutoff frequencies of the fundamental and high-order modes

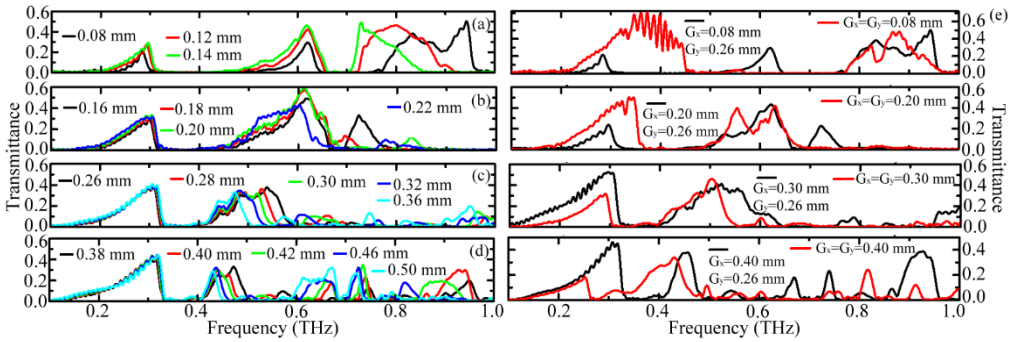

Fig. 5. Transmittance spectra for 30 MRA layers with the same 0.26 mm G_y but different G_x values: (a) 0.08–0.14, (b) 0.16–0.22, (c) 0.26–0.36, and (d) 0.38–0.50 mm. (e) The comparison of transmittance spectrum between two cases of G_x=G_y and G_x≠G_y.

OSA CONTINUUM

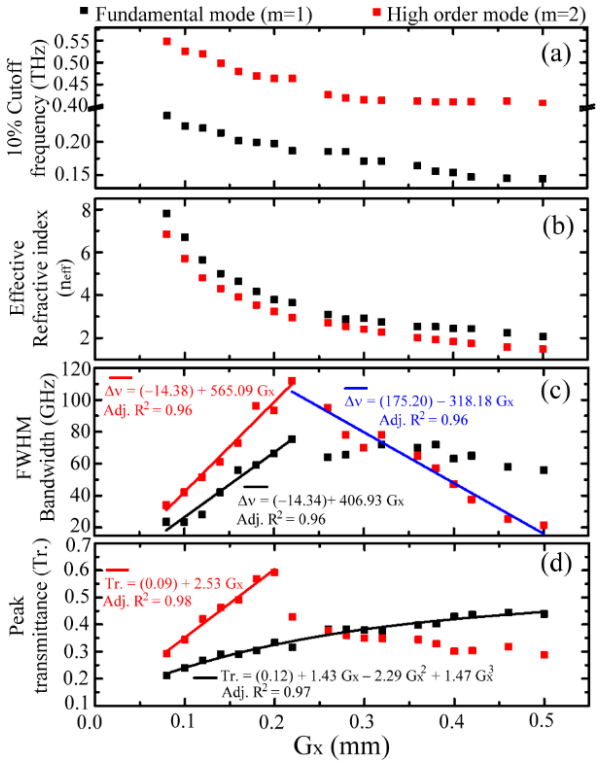

Fig. 6. G_x-dependent waveguide parameters of (a) cutoff frequency, (b) effective refractive index, (c) bandwidth, and (d) peak transmittance.

perform the redshift effect with the increased G_x, thereby approaching to a PPWG that depends on the gap size between two metal reflection plates [17]. However, the refractive index of a G_x interspace channel is not as simple as the PPWG hollow core with an air refractive index (i.e., 1.0), because the inner reflection walls are constructed from the MRA line structures [i.e., the metal rods in the Y–Z plane in Fig. 1(a)] instead of uniform metal surfaces.

The waveguide refractive indices of TM modes (n_{eff}) that depend on different G_x (0.08–0.50 mm) can therefore be estimated on the basis of the effective medium concept in Eq. (1) and the cutoff frequencies in Fig. 6(a). Figure 6(b) shows the estimation results of n_{eff} and indicates that a small G_x performs the high n_{eff} given the apparent phase delay of THz wave reflection from the MRA line structures. When G_x extends nearly or larger than 0.50 mm to deliver the 2nd TM modes, the related n_{eff} approaches 1.0 and resembles the hollow core space of a PPWG. The high n_{eff} values imply that the high waveguide dispersion of MRA–TM modes originates from the narrow interspace of G_x due to the strong phase retardation of THz waves among the metal rods.

The effective medium concept successfully expresses the spectral shift [Fig. 6(a)] and waveguide dispersion [Fig. 6(b)] when the 12 G_x interspace channels are defined as one PPWG-like waveguide that is integrated by 13 MRA lines. The waveguide-mode bandwidths based on the full width at half maximum (FWHM) and the corresponding peak transmittance that depends on G_x are further observed from Fig. 5 (a)–(d), as shown in Figs. 6(c) and 6(d), respectively. The G_x-dependent performances between the 1st and 2nd TM waveguide modes are distinct and shown as the black and red squares for the FDTD calculation results, respectively. For the 1st TM waveguide mode, the FWHM bandwidth is proportional to G_x in the range of 0.08–0.22 mm, which is illustrated as the fitting curve [black line in Fig. 6(c)] and saturated around 60 GHz. The highest transmittance

OSA CONTINUUM

(i.e., the peak transmittance) of the 1st TM mode also increases for the increment of G_x, which is denoted as *Tr.* and fit by the black curve in Fig. 6(d). The *Tr.* trend of the 1st MRA–TM mode is proportional to G_x or ${G_x}^3$, which is consistent to that of one PPWG that depends on its hollow core space [20]. Therefore, increasing G_x interspace enables the widest bandwidth and highest peak transmittance for the 1st TM mode. However, the 2nd TM mode has abnormal transportation properties when G_x interspace is increased; these properties are opposite to those of the 1st TM mode and summarized as the red squares in Figs. 6(c) and 6(d). The 0.20–0.22 mm G_x performs the widest bandwidth and peak transmittance for the 2nd TM mode. When G_x increases from 0.08 mm to 0.20 mm, the peak transmittance and bandwidth of the 2nd TM mode evidently increase due to the reduction of metal cross section, thereby decreasing the waveguide loss of the THz waves. Conversely, further increasing the interspace of G_x to over 0.20–0.22 mm decays the bandwidth and peak transmittance of the 2nd TM mode because the Z-axial confinement of the TM high-order modes is destroyed [Fig. 4(a)]. It indicates that the MRA structure with the exact G_x values can promote the waveguide capabilities both on the transmission and lateral confinement. The fitting curves of the red lines in Figs. 6(c) and 6(d) illustrate that the theoretical waveguide capabilities of the 2nd TM mode for the bandwidth and spectral peak transmittance are proportional to 0.08–0.22 mm G_x. For G_x larger than 0.20–0.22 mm, the trend of the 2nd-mode bandwidth is different from that on the peak transmittance. The bandwidth of the 2nd TM mode is inversely proportional to 0.22–0.50 mm G_x, which is illustrated as the linear fitting curve of the blue line in Fig. 6(c). The peak transmittance of the 2nd TM mode seriously decays when G_x increases from 0.20 mm to 0.22 mm, as shown in Fig. 6(d).

Figure 7(a) presents the G_x-dependent modal patterns of the 2nd TM waveguide modes at the corresponding spectral peak frequencies. Four G_x interspaces taken as examples in the modal pattern calculation are 0.12, 0.20, 0.30, and 0.46 mm [Fig. 7(a)] with spectral peak frequencies of

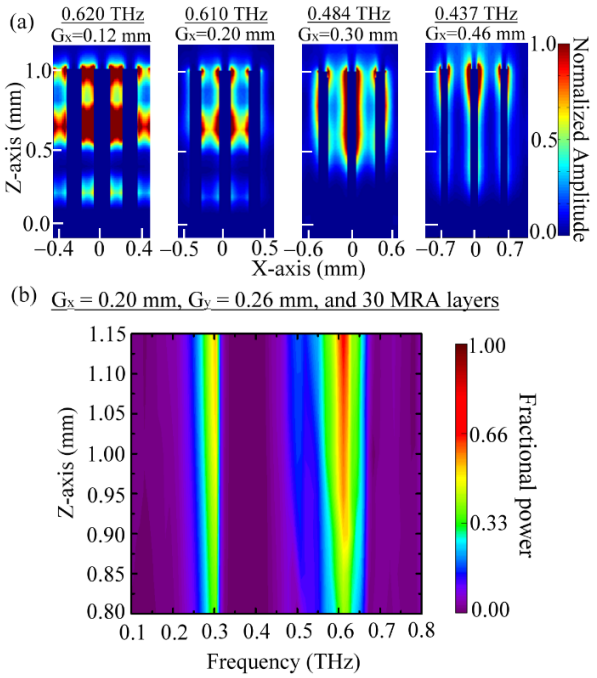

Fig. 7. (a) Electric field distributions at the 30th MRA layer for the transmission peaks of the 2nd TM modes dependent on G_x. (b) Frequency-dependent modal power fraction of the 30-layer MRA waveguide (G_x=0.20 mm, G_y=0.26 mm).

OSA CONTINUUM

0.620, 0.610, 0.484, and 0.437 THz for the 30-layer MRA propagation, respectively. For the 0.12 mm G_x, the 0.620 THz wave is strongly bound on the metal rod surface along the Y-axial propagation or inside the G_x interspace channels. The field of 0.610 THz wave strongly bound by metal rods still occurs for the large G_x interspace at 0.20 mm. When G_x is increased to 0.30 mm and 0.46 mm, the metal surface-bound fields of the 2nd spectral peak are apparently separated inside the G_x interspaces with low amplitude distribution. From Figs. 6(d) and 7(a), the 0.20 mm G_x makes the 2nd TM mode wave have the highest transmittance and the strongest confinement. The frequency-dependent modal power fraction of the 30-layer propagation is illustrated in Fig. 7(b) for the 0.20 mm G_x MRA. Obviously, the spectral width shrinks for the MRA-confined THz waves with high power fractions (>0.6) inside the MRA, which is compared by that of the MRA waveguide with a symmetric interspace, G_x=G_y=0.26 mm [Fig. 4(a)]. It represents that THz waves with one narrow bandwidth in 0.60–0.62 THz can be confined to be guided, corresponding to the spectral peak transmittance of the 2nd TM waveguide mode [Fig. 5(b)]. Other waves with frequencies in 0.10–0.60 THz and higher than 0.62 THz, as shown in Fig. 7(b), are not confined to be guided by the MRA because the power fraction is approximately constant along the Z-axis. The high distinctions of lateral confinement and waveguide transmittance at the 2nd TM mode spectrum is consequently derived from the asymmetric interspaces, which are 0.20 mm G_x and 0.26 mm G_y.

Figure 8(a) shows the spectral peak transmittances of the 2nd TM modes for the 0.12, 0.20, 0.30, and 0.46 mm G_x and their propagation lengths with 30–70 MRA layers. The peak transmittances of the 2nd TM modes for small G_x interspaces at 0.12, 0.20, and 0.30 mm are exponentially decayed by the added MRA layers, which are illustrated as the fitting curves of the red lines in Fig. 8(a). For a large G_x interspace at 0.46 mm, the peak transmittance of the 2nd TM mode fluctuates around 0.3 without the trend of exponential decay with the added MRA layers. As shown by the modal field observation in Fig. 7(a), such transmittance fluctuation with the given MRA propagation length results from the low fractional power of 0.437 THz wave inside the 0.46 mm G_x MRA structure. The sufficiently small G_x interspaces at 0.12, 0.20, and 0.30 mm make the MRA structure have the same attenuation characteristic of a normal dielectric waveguide. Among these four G_x interspaces, 0.20 mm G_x performs the highest transmittance of the 2nd TM mode, and the longest propagation length can be extended up to 105 MRA layers as the peak transmittance reduces to 0.1. The propagation length with 105 MRA layers, which is estimated from the fitting curves in Fig. 8(a), is approximately 30 mm.

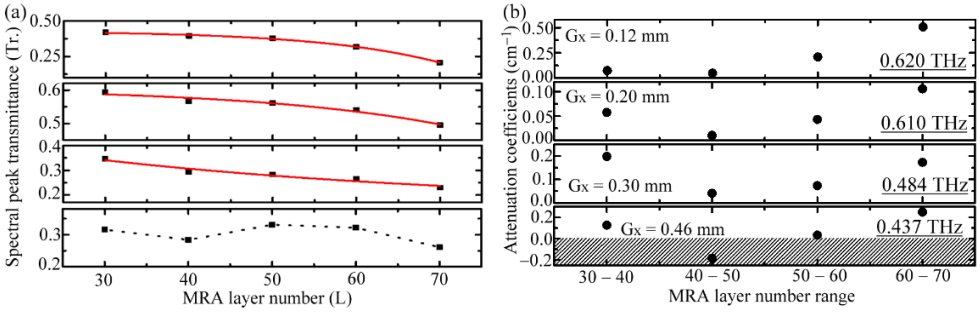

Fig. 8. (a) Relationship between the peak transmittance of the 2nd TM mode and the number of transmitted MRA layer. (b) Relationship between the attenuation coefficients of the 2nd TM mode and the waveguide intervals behind the 30th MRA layer.

We consider 10 MRA layers as one waveguide interval from Fig. 8(a) and analyze the peak attenuation coefficients of four different waveguide intervals behind the 30th MRA layer [Fig. 8(b)]. The 10 MRA layers equal a 3.94 mm-long propagation length, corresponding to 5–9

OSA CONTINUUM

λ of the spectral peak frequency for the 2nd TM mode in Fig. 7(a). The propagation loss, resulted from the beam divergency without being confined by the MRA, can thus be observed along the 10-MRA-layer interval because the interval length is much larger than the Raleigh ranges of those waves in Fig. 7(a). Because the across section of waveguide medium is not continuous like a metal-wire-grid or a slit array, i.e., one MRA layer in X-Z plane, different G_x interspaces certainly cause different beam divergency, thereby leading different delivery performance or propagation loss of THz waves among the 10 MRA layers. The attenuation coefficients are obtained from the equation $[ln(Tr._1/Tr._2)]/[2(L_2-L_1)]$, where $L_{1,\,2}$ indicates two waveguide lengths for different numbers of MRA layer, and $Tr._{1,\,2}$ indicates the related transmittance at different numbers of MRA layer. Figure 8(b) shows that the coefficients of waveguide attenuation evidently vary among these intervals because of the variations of the average beam divergency and spatial confinement. Therefore, an MRA is absolutely different from those isotropic or uniform dielectric media when an MRA waveguide performance is defined by the propagation loss. The analysis in Fig. 8(b) shows that the waveguide intervals between the 40th and 50th MRA layers for these four G_x interspaces [Fig. 7(a)] have the lowest metal rod attenuation and the coefficients are less than 0.05 cm^{-1}. To sustain the 2nd TM mode for the longest propagation length of up to 70 MRA layers, the G_x interspace around 0.20 mm is ideal for the MRA waveguide and performs attenuation of less than 0.1 cm^{-1}. For G_x smaller than 0.20 mm, a long waveguide is not performed because of the large cross section of metal, thereby causing an extremely high waveguide loss of THz waves. Although the large G_x values above 0.20 mm have relatively lower attenuation than that of 0.12 mm G_x, the MRA cannot well control the 2nd TM waveguide mode on the lateral confinement.

4. Conclusion

The MRA structure is numerically demonstrated by FDTD calculation as one THz waveguide. The fundamental and high-order TM waveguide modes are distinctly found in 0.1–1 THz along the 30-layer MRA propagation. For the uniform metal rod interspace, the high-order waveguide modes divided by the Bragg-like reflection originate from the sufficiently long metal rod length. For 1-mm-long rod in an MRA, assembling the metal rods with an asymmetric interspace (i.e., $G_x \neq G_y$) is presented as the critical stratagem to tailor the high-order TM waveguide mode with optimal transportation efficiency of THz waves. We consider the 0.16 mm D, 0.26 mm G_y, and 1-mm-long rod length as the geometrical basis to adjust G_x in 0.08–0.50 mm and find apparent spectral redshift by increasing G_x for the MRA–TM modes. Such a spectral shift that is inversely proportional to the G_x interspace resembles the PPWG performance on the TM waveguide modes that depend on the hollow core spaces. The G_x interspace channel constructed by two MRA lines is thus the structural unit for determining the modal properties of TM–THz waves based on the effective medium concept. On the basis of 0.16 mm D, 0.26 mm G_y, and 1-mm-long rod, the 2nd TM waveguide mode through 30-layer MRA propagation is stably performed in 0.4–0.7 THz for 0.08–0.50 mm G_x. Based on the observation of G_x-dependent modal field properties, the MRA-guided THz field is exactly bound on the metal rod surface with the lowest waveguide loss or the high transmittance; thus, when G_x approaches 0.20 mm, the efficiency of THz waveguide, which is defined by the transmittance, bandwidth, and attenuation, can be optimized. The longest waveguide length and widest bandwidth can consequently be obtained when the symmetric interspace of 0.26 mm is modified as the asymmetric one with 0.20 mm G_x and 0.26 mm G_y. The natural confinement performance of the 2nd TM mode at the MRA–air interface enables the MRA structure to be feasible for a THz slab dielectric waveguides.

Funding

Japan Society for the Promotion of Science (JSPS) (JP16K17525).

OSA CONTINUUM

Acknowledgment

This work was supported by grants-in-aid for scientific research from the Ministry of Science and Technology of Taiwan (MOST107-2221-E-006-183-MY3) and Japan Society for the Promotion of Science (JSPS, KAKENHI, JP16K17525).

References

1. W. L. Barnes, A. Dereux, and T. W. Ebbesen, "Surface plasmon subwavelength optics," Nature **424**(6950), 824–830 (2003).
2. F. J. Garcia-Vidal, L. Martin-Moreno, T. W. Ebbesen, and L. Kuipers, "Light passing through subwavelength apertures," Rev. Mod. Phys. **82**(1), 729–787 (2010).
3. D. K. Gramotnev and S. I. Bozhevolnyi, "Plasmonics beyond the diffraction limit," Nat. Photonics **4**(2), 83–91 (2010).
4. A. V. Kabashin, P. Evans, S. Pastkovsky, W. Hendren, G. A. Wurtz, R. Atkinson, R. Pollard, V. A. Podolskiy, and A. V. Zayats, "Plasmonic nanorod metamaterials for biosensing," Nat. Mater. **8**(11), 867–871 (2009).
5. J. B. Pendry, L. Martin-Moreno, and F. J. Garcia-Vidal, "Mimicking surface plasmons with structured surfaces," Science **305**(5685), 847–848 (2004).
6. S. H. Kim, S. S. Oh, K. J. Kim, J. E. Kim, H. Y. Park, O. Hess, and C. S. Kee, "Subwavelength localization and toroidal dipole moment of spoof surface plasmon polaritons," Phys. Rev. B **91**(3), 035116 (2015).
7. C. R. Williams, S. R. Andrews, S. A. Maier, A. I. Fernández-Domínguez, L. Martín-Moreno, and F. J. García-Vidal, "Highly confined guiding of terahertz surface plasmon polaritons on structured metal surfaces," Nat. Photonics **2**(3), 175–179 (2008).
8. B. Ng, J. Wu, S. M. Hanham, A. I. Fernández-Domínguez, N. Klein, Y. F. Liew, M. B. H. Breese, M. Hong, and S. A. Maier, "Spoof plasmon surfaces: a novel platform for THz sensing," Adv. Opt. Mater. **1**(8), 543–548 (2013).
9. B. Gupta, S. Pandey, and A. Nahata, "Plasmonic waveguides based on symmetric and asymmetric T-shaped structures," Opt. Express **22**(3), 2868–2880 (2014).
10. J. Keller, C. Maissen, J. Haase, G. L. Paravicini-Bagliani, F. Valmorra, J. Palomo, J. Mangeney, J. Tignon, S. S. Dhillon, G. Scalari, and J. Faist, "Coupling surface plasmon polariton modes to complementary THz metasurfaces tuned by inter meta-atom distance," Adv. Opt. Mater. **5**(6), 1600884 (2017).
11. N. R. Han, Z. C. Chen, C. S. Lim, B. Ng, and M. H. Hong, "Broadband multi-layer terahertz metamaterials fabrication and characterization on flexible substrates," Opt. Express **19**(8), 6990–6998 (2011).
12. M. A. Seo, H. R. Park, S. M. Koo, D. J. Park, J. H. Kang, O. K. Suwal, S. S. Choi, P. C. M. Planken, G. S. Park, N. K. Park, Q. H. Park, and D. S. Kim, "Terahertz field enhancement by a metallic nano slit operating beyond the skin-depth limit," Nat. Photonics **3**(3), 152–156 (2009).
13. Y. M. Bahk, S. Han, J. Rhie, J. Park, H. Jeon, N. Park, and D. S. Kim, "Ultimate terahertz field enhancement of single nanoslits," Phys. Rev. B **95**(7), 075424 (2017).
14. J. W. Lee, T. H. Park, P. Nordlander, and D. M. Mittleman, "Terahertz transmission properties of an individual slit in a thin metallic plate," Opt. Express **17**(15), 12660–12667 (2009).
15. B. You, C. C. Peng, J. S. Jhang, H. H. Chen, C. P. Yu, W. C. Lai, T. A. Liu, J. L. Peng, and J. Y. Lu, "Terahertz plasmonic waveguide based on metal rod arrays for nanofilm sensing," Opt. Express **22**(9), 11340–11350 (2014).
16. B. You, D. Liu, T. Hattori, T. A. Liu, and J. Y. Lu, "Investigation of spectral properties and lateral confinement of THz waves on a metal-rod-array-based photonic crystal waveguide," Opt. Express **26**(12), 15570–15584 (2018).
17. D. Sievenpiper, L. Zhang, R. F. J. Broas, N. G. Alexopolous, and E. Yablonovitch, "High-impedance electromagnetic surfaces with a forbidden frequency band," IEEE Trans. Microw. Theory Tech. **47**(11), 2059–2074 (1999).
18. M. A. Kats, D. Woolf, R. Blanchard, N. Yu, and F. Capasso, "Spoof plasmon analogue of metal-insulator-metal waveguides," Opt. Express **19**(16), 14860–14870 (2011).
19. R. Halir, P. J. Bock, P. Cheben, A. Ortega-Moñux, C. Alonso-Ramos, J. H. Schmid, J. Lapointe, D.-X. Xu, J. G. Wangüemert-Pérez, I. Molina-Fernández, and S. Janz, "Waveguide sub-wavelength structures: a review of principles and applications," Laser Photon. Rev. **9**(1), 25–49 (2015).
20. D. K. Cheng, *Field and Wave Electromagnetics*, 2nd ed. (Addison-Wesley, 1989), chap. 5.